SUPPORTING INFORMATION FOR

Raman Characterization of Nanoparticle Transport in Microfluidic Paper-Based Analytical Devices (µPADs)

*Rebecca Halvorson Lahr, Grant C. Wallace, Peter J. Vikesland**

Department of Civil and Environmental Engineering and Institute of Critical Technology and Applied Science (ICTAS), Virginia Tech, 418 Durham Hall, Blacksburg, VA 24060-0246

*Corresponding author E-mail: pvikes@vt.edu; 540-231-3568; Fax: 540-231-7916

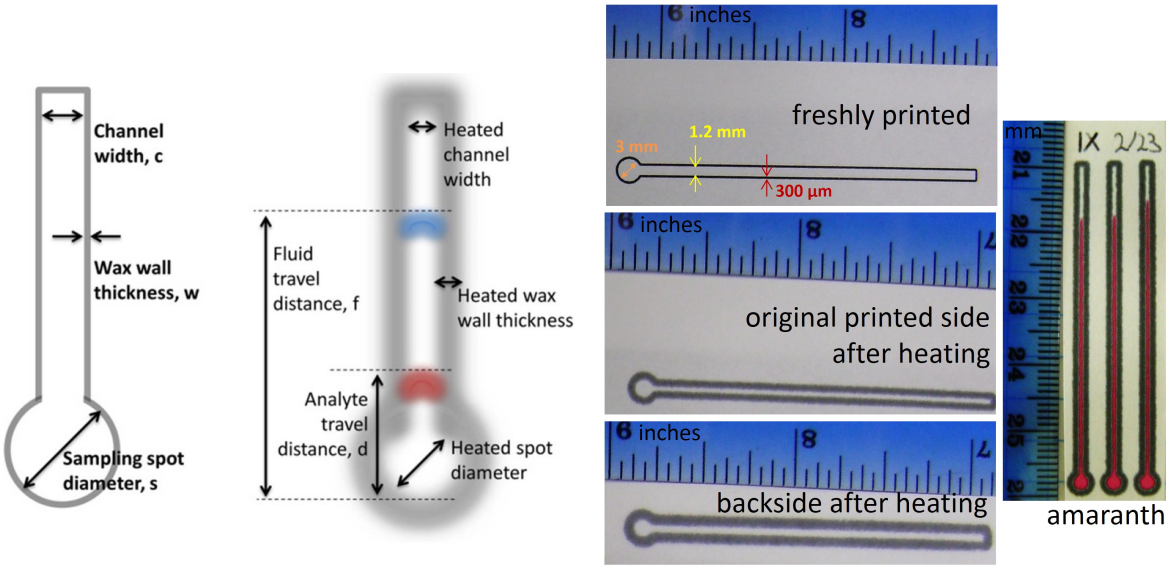

Figure S1. The µPAD dimensions describe measurements designed in Adobe Photoshop software (left). Heating the papers to re-flow the wax caused lateral as well as axial wax spreading, thus creating narrower channels in the tested µPADs than the original printed dimensions. Photographs of printed, heated µPADs containing amaranth dye demonstrate the ability of wax to contain aqueous solutions (right).

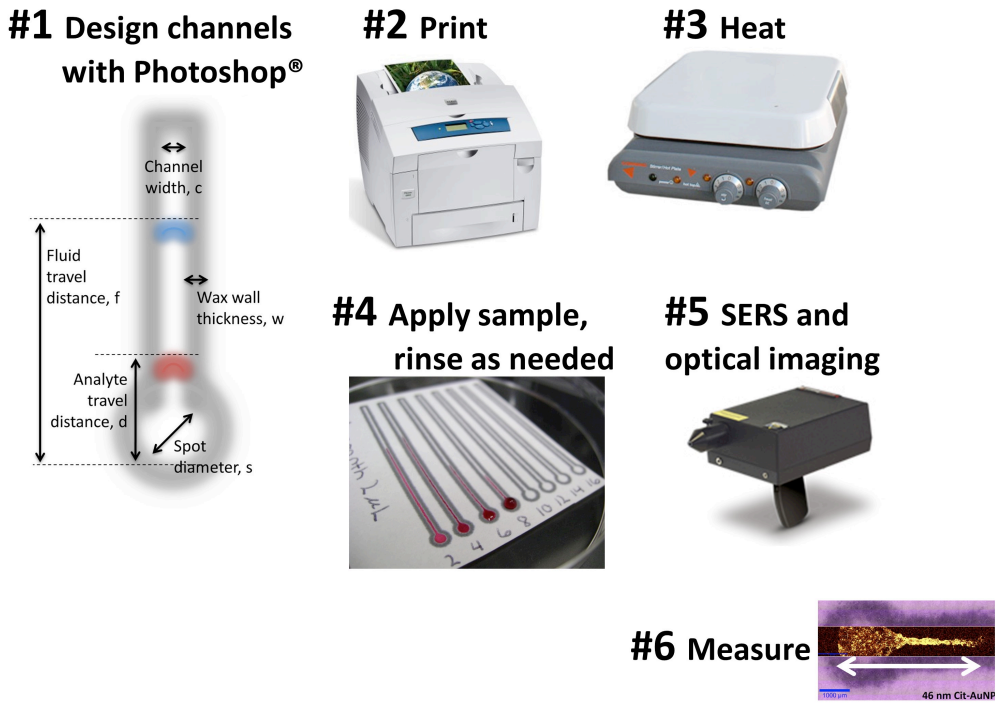

Figure S2. Flow chart of experiments performed for this work.

Table S1. Nanoparticle synthesis procedures. AuNP and AgNP were produced with the desired coatings using published protocols.

Particle	Synthesis Method	Refs.
15 nm cit-AuNP	Spiked 10 mL of 38.8 mM sodium citrate into 100 mL of hot 1 mM $HAuCl_4$ and refluxed until particles formed.	[1]
46 nm cit-AuNP	Spiked 1.6 mL of Abs = 3.0 of 15 nm Cit-AuNP seeds and 0.44 mL of 38.8 mM sodium citrate into 100 mL of hot 0.254 mM $HAuCl_4$. Refluxed until particles formed (1 hr).	[1]
15, 46, 64 nm BSA-cit-AuNP	Spike 0.1 mg BSA per mL of the appropriate size of Cit-AuNP.	[2]
46 nm MixPEG-cit-AuNP	Added dropwise 1 μM HS-PEG-COOH to 46 nm Cit-AuNP to achieve 3000 COOH-PEG molecules per AuNP. Particles were then mixed for 15 minutes before adding excess 10 μM HS-PEG-OCH_3 to achieve 16000 OCH_3-PEG molecules per AuNP. After mixing for an additional 15 minutes, AuNP were centrifuged and washed several times to remove excess PEG. The OCH_3-PEG coated 46 nm AuNP (46 nm OCH_3-PEG-cit-AuNP) and COOH-PEG coated 46 nm AuNP (46 nm COOH-PEG-cit-AuNP) were prepared similarly as 46 nm MixPEG-cit-AuNP except that a single type of PEG was used at a concentration of 19000 PEG molecules per AuNP.	[3]
46 nm PEG-MGITC-cit-AuNP and 46 nm PEG-RBITC-cit-AuNP	Added 300 dye molecules per AuNP via syringe to a vortexing tube of 46 nm Cit-AuNP, incubated overnight at 4°C, and pegylated as described previously.	[3]
46 nm DNA-PEG-MGITC-cit-AuNP	Added 50 μL of 4 mg/mL EDC in PBS and 55 μL of 10 mg/mL sulfo-NHS in PBS to 1 mL of 10^{10} 46 nm PEG-MGITC-AuNP in PBS buffer. Twelve nmol of oligonucleotide were then added in 200 μL to the AuNP solution before shaking overnight at room temperature, while protected from light. Excess reagents were removed by centrifugation (5 rounds at 10000 × g for 10 minutes each). All PEG coated AuNP were stored in the dark at 4°C in 50% (v/v) ethanol-water solutions and re-suspended in nanopure water before use.	[3]
46 nm PEG-Peptide-cit-AuNP	A 0.1 mL spike of 380 μM peptide was added to 50 mL of 46 nm Cit-AuNP to achieve 10000 peptides per AuNP. After stirring for 2 hours at room temperature, 100 μM OCH_3-PEG-HS was added to a molar ratio of 9000 PEG molecules per AuNP. The solution was incubated at room temperature overnight.	[3]
36 nm EDTA-AgNP	Vigorously shook a mixture containing 100 mL of 0.16 mM EDTA and 4 mL of 0.1 M NaOH spiked with 1 mL of 26 mM $AgNO_3$.	[4]
8 nm PVP10K-AgNP and 8 nm PVP55K-AgNP	PVP (1.5 g of 10 kDa or 55 kDa) was dissolved in 280 mL water, mixed with 9 mL of 0.1 M $AgNO_3$, stirred 5 min, spiked with 11 mL of 0.08 M ice-cold sodium borohydride, and centrifuged to remove excess reagent.	[5]
41 nm PVP10K-AgNP and 40 nm PVP55K-AgNP	PVP was dissolved in ethylene glycol (1.5 g of 10 kDa in 75 mL or 20 g of 55 kDa in 50 mL), mixed with $AgNO_3$ (0.05 g or 1.5 g), heated under stirring (120°C for 1 hr or 140°C for 24 hr), and dialyzed or centrifuged to remove unbound species.	[4]
AuNR	$HAuCl_4$ was mixed with CTAB and reduced with sodium borohydride to produce 1.5 nm spherical AuNP. AuNP were further grown in the presence of CTAB, $AgNO_3$, $HAuCl_4$, and ascorbic acid overnight at 33 ºC. Centrifugation removed excess CTAB.	

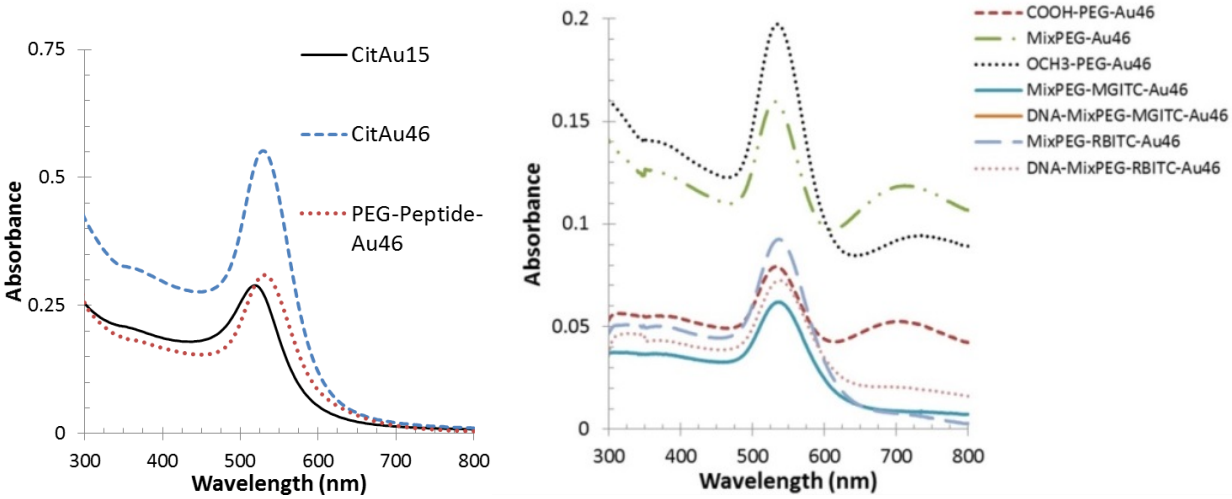

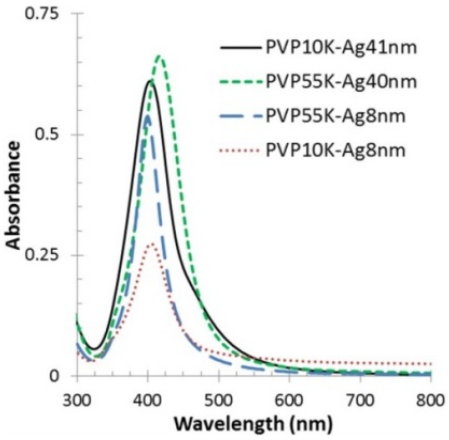

Sample	LSPR (nm)	Concentration (Haiss eqn; µM)
15 nm cit-AuNP	519	8000
46 nm cit-AuNP	529	70
15 nm BSA-cit-AuNP		
46 nm BSA-cit-AuNP	535	70
64 nm BSA-cit-AuNP	546	20
46 nm OCH_3-PEG-cit-AuNP	535	10
46 nm COOH-PEG-cit-AuNP	532	7
46 nm OCH_3/COOH-PEG-cit-AuNP	531	10
46 nm MixPEG-MGITC-cit-AuNP	537	4
46 nm MixPEG-RBITC-cit-AuNP	536	6
46 nm DNA-MixPEG-MGITC-cit-AuNP	538	100
40 nm PVP10K-AgNP	419	400
40 nm PVP55K-AgNP	416	40 nM
8 nm PVP55K-AgNP	399	2000 nM
8 nm PVP10K-AgNP	405	2000 nM

Figure S3. UV-Vis spectra and LSPR maximum of aqueous nanoparticle solutions.[6]

Table S2. Raman peak assignments for the 55-398 cm^{-1} region.

SERS peaks (cm^{-1})	**Reported assignments**	Reference
120-158	gold surface binding with I^-	[7]
152	S-S-S and S-S (with 216 cm^{-1} and 471 cm^{-1})	[8]
180	gold surface binding with SO_4^{-2}	[9]
181-209	gold surface binding with Br^-	[7,9]
216	S-S-S and S-S (with 152 cm^{-1} and 471 cm^{-1})	[8]
225-227	Ag(0) - N	[10]
230-260	Plasmon - phonon coupling	[11]
235	Au(0) – S of SCN	[7]
240	Ag(0) - N of benzyolpyridine	[10]
240-250	Ag(0) – Cl^-	[9]
245-275	Ag(0) – Cl^-	[7,9]
250-260	Cyano groups binding to a gold surface through the nitrogen atom	[9]
254	S-S-S	[8]
260	Extramolecular stretching of Au-C	[12]
260	Au-S	[13]
261	S-S-S	[8]
267	Au(0)-S of cysteine	[14]
270-310	Au-S	[8]
296	Au-S	[15]
300	Au(0)-N of NCS	[7]
300 and 380	Au(0)-CN	[7]
471	S-S-S and S-S (with 152 cm^{-1} and 216 cm^{-1})	[8]
330	Extramolecular stretching of Au–O	[12]

Table S3. Specific instrument parameters used to collect Raman and SERS spectra of each analyte. All spectra were collected in paper using a 785 nm laser, 300 grooves per mm grating, and 10× microscope objective.

Sample	Acquisition time (seconds)	Number of averaged spectra	Approximate laser power (mW)
Cellulose	1	10	>100
Wax melted on paper	1	10	>100
Amaranth	1	10	> 100
15 nm Cit-AuNP	0.05	120000 spectra over a 6000 µm × 1000 µm Raman spectral map	< 0.3
46 nm Cit-AuNP	0.01	145000 spectra over a 7000 µm × 1000 µm Raman spectral map	< 0.3
DNA-PEG-MGITC-cit-AuNP	0.01	40000 spectra over a 2000 µm × 2000 µm Raman spectral map	< 5
AuNR	0.01	40000 spectra over a 2000 µm × 2000 µm Raman spectral map	< 5
46 nm PEG-MGITC-cit-AuNP	0.01	2500 spectra over a 1000 µm × 1000 µm Raman spectral map	< 25
46 nm PEG-RBITC-cit-AuNP	0.01	2500 spectra over a 1000 µm × 1000 µm Raman spectral map	< 25
46 nm BSA-cit-AuNP	0.05	80000 spectra over a 8000 µm × 500 µm Raman spectral map	< 0.6
64 nm BSA-cit-AuNP	0.05	80000 spectra over a 8000 µm × 500 µm Raman spectral map	< 0.6
41 nm PVP10K-AgNP	0.05	20000 spectra over a 2000 µm × 500 µm Raman spectral map	< 0.6

Characterization of wax ink, papers, and µPADs.

The Xerox ColorQube ink melts below 120 ºC, a lower re-flow temperature than the original Xerox ink, and is likely composed of carbon black pigment and hydrophobic polymer or hydrocarbon mixture (**Table S4**).[16-21] The wax re-flow process caused wax spreading within the paper from an initial printed wax dimension of 0.3 mm to a heated dimension of approximately 0.8 mm to 1.1 mm for the back of the paper and the original printed side respectively (**Figure S1**).[16] FE-SEM shows smooth regions on the cellulose fibers after wax re-flow that are not observed on the cellulose fibers without wax (**Figure S4**).

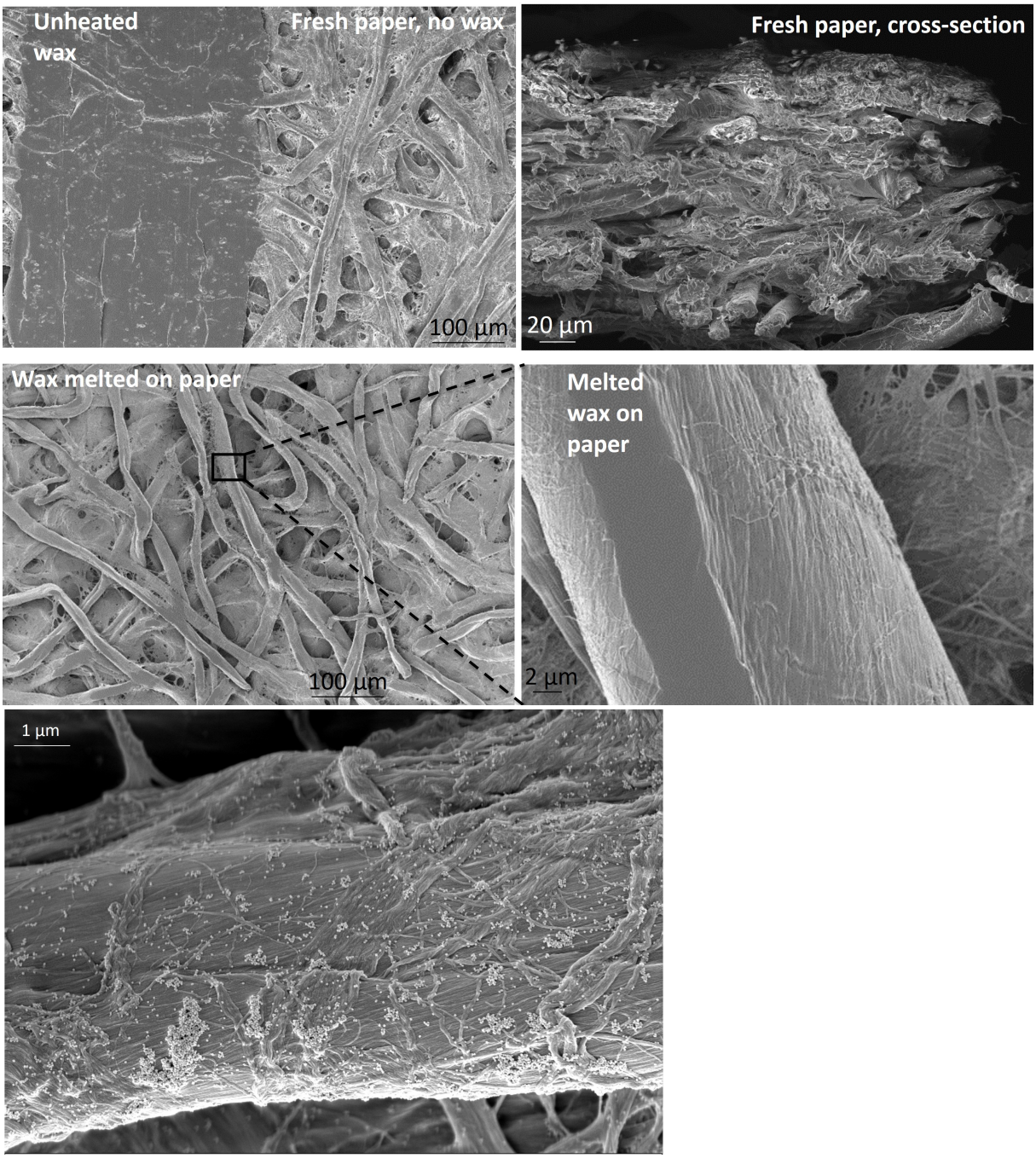

Figure S4. FE-SEM images of Whatman grade 1 chromatography paper before and after heating including a) an un-heated wax-printed paper, b) a cross-section of chromatography paper without wax (sample frozen in liquid nitrogen, cut with a cold scalpel blade while still frozen, mounted onto an SEM stub, and sputter coated with Au for analysis), c) melted wax on paper, d) a close-up image of a wax-coated cellulose fiber, and e) a cellulose fiber on which 40 nm cit-AuNP were deposited. The relative scale of the nanomaterials with respect to the "sinusoidal corrugated" cellulose fiber surface, assumed to be smooth and flat by the DLVO model, is demonstrated.[22]

Table S4. Assignments for Raman peaks displayed by wax ink. The composition of the phase changing ink is proprietary, but likely contains carbon black pigment and a hydrophobic hydrocarbon mixture or polymer.[16,19-21]

Peak (cm^{-1})	Molecular Vibration	Reference
569	Ring vibrations, NO_2, nitric acid esters, aromatics	[23,24]
746	Ring breathing mode, CH deformation, CC, earth wax	[24,25]
818	C-C stretching, cyclohexane, ring vibration	[23,24]
889	Methylene rocking, cyclopentane, ring vibration, CH_2, COC, unsaturated and saturated waxes	[23-25]
904	C-O-C, ring vibrations	[23,24]
1213	Aromatic stretching, C-N stretching, methyl rocking, COC, C=C-O-C	[23,24]
1241	C=C-O-C, COC, phosphate, NO_2,	[23,24]
1287	Aromatics, nitric acid esters, pyrimidine bases, phosphodiesters	[23,24]
1333-1351	Carbon black, branched hydrocarbon chains, phenyl, CH_3, CH_2, CH, NO_2	[24,26,27]
1454	CH_3 and CH_2 modes, phospholipids, cyclopentane derivatives, unsaturated and saturated waxes	[23-25,28]
1564	COO-, purine bases, ring breathing modes, N-NO_2	[23,24]
1580	Carbon black	[26,27]

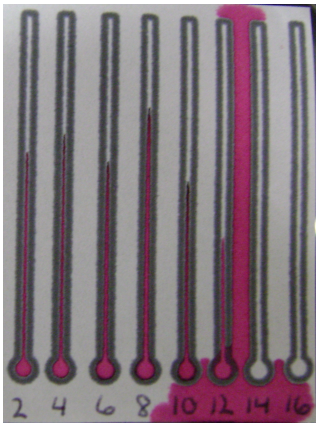

Figure S5. Wax-printed paper channels (1.2 mm channel width, 0.3 mm wax walls, and 3 mm sampling spots, original printed side up in a Petri dish) typically contained amaranth solutions up to a volume of 12 µL. Samples > 12 µL typically spilled out of channels.

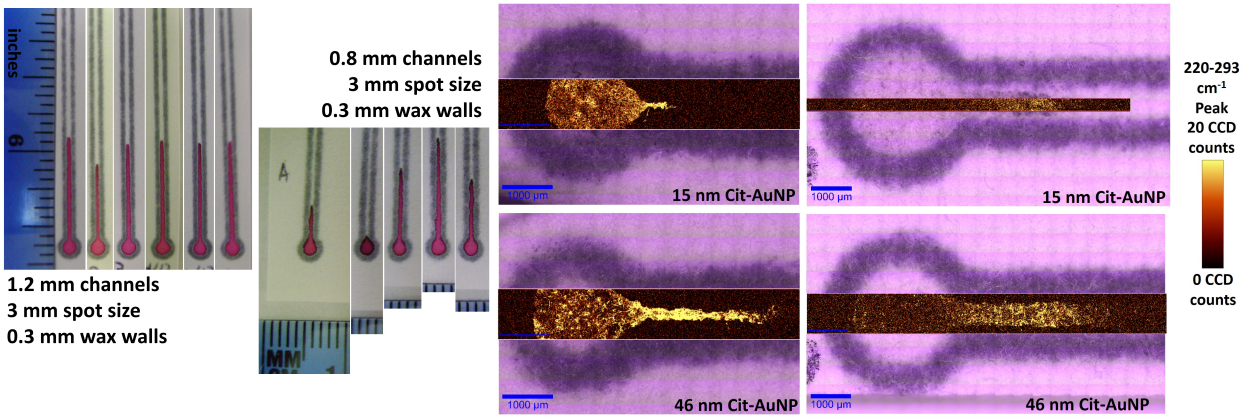

Figure S6. Normal Raman spectral maps image the topography of the cellulose fibers and deposition patterns of fluorescent species even within the same wax-printed paper channel (Figure S7), while the SERS spectral maps are generated with a low enough laser power such that only nanomaterials display spectra. Optical images collected using a 10× microscope objective (purple) and overlaid SERS spectral maps demonstrate nanoparticle deposition patterns within the wax-printed cellulose channels. SERS Spectral images were collected with a 785 nm laser, 300 gr/mm grating, 10× microscope objective, 0.05 seconds per spectrum, and 5 to 10 spectra per µm. Channel dimensions were chosen to produce the most consistent fluid flow and strong SERS signals. Narrow channels concentrated samples to facilitate strong SERS signals, but the spread of the wax caused channels narrower than 1.2 mm to periodically constrict flow as observed in the photographs on the left. Nanoparticles are still observed within channels over 1.2 mm wide, though longer acquisition times, SERS tags bound to nanoparticles, or higher laser powers are often required.

Contact angle measurements were collected for water droplets on the wax ink block, heated and unheated wax printed on chromatography paper, and water-soaked printed papers. As suggested by Noh and Phillips, wax-printed paper absorbs water droplets if given sufficient time after deposition; hence, water droplets were analyzed immediately after placement on the sample.[29] After heating for wax re-flow, the original wax-printed side of the paper (front) had a higher contact angle than the back of the paper when both samples were not pre-wetted, indicating that the original printed side retains most of the wax thus making it more hydrophobic (**Table S5**). The hydrophobicity and the clear difference in the amount of wax spreading between the two sides of the paper explain the dependence of solution flow upon the orientation of the paper (original printed side up or down). Contact angles were consistently lower for papers that were pre-wetted before measurements were collected. The water adsorption properties of cellulose are well documented, and although high purity cotton cellulose such as that in Whatman grade 1 chromatography paper sorbs less water than other types of cellulose,[30] the dry or pre-wetted state remains an important variable to hold constant or engineer to improve functionality of wax-printed paper devices. For consistency, the nanoparticle transport

experiments reported here were conducted with dry papers as purchased and stored on a lab bench.

Table S5. Contact angle (degrees) measurements for wax on cellulose.

	Advancing Contact Angle (°)		**Receeding Contact Angle (°)**	
	dry sample	pre-wetted sample	dry sample	pre-wetted sample
Black Wax	113±6		94±7	
Unheated wax-printed paper	113±2	110±2	99±2	92±4
Heated wax-printed paper, original printed side	142±3	106±24	115±22	92±7
Heated wax-printed paper, back of paper	138±1	117±5	107±1	96±2
Paper (no wax)	0	0	0	0

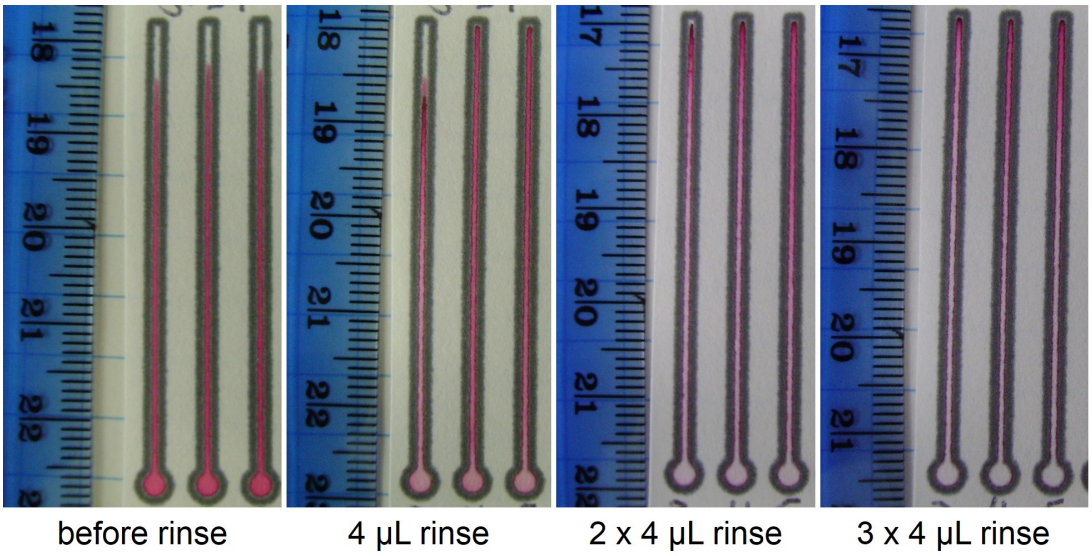

Figure S7. Amaranth dye deposited within the sampling spot (2 µL) travels with the aqueous phase through the paper. After at least 10 minutes of drying time and a 4 µL water rinse placed in the sampling spot, the amaranth is rinsed further along the channel. Additional rinse steps further concentrate the amaranth dye at the end of the channel.

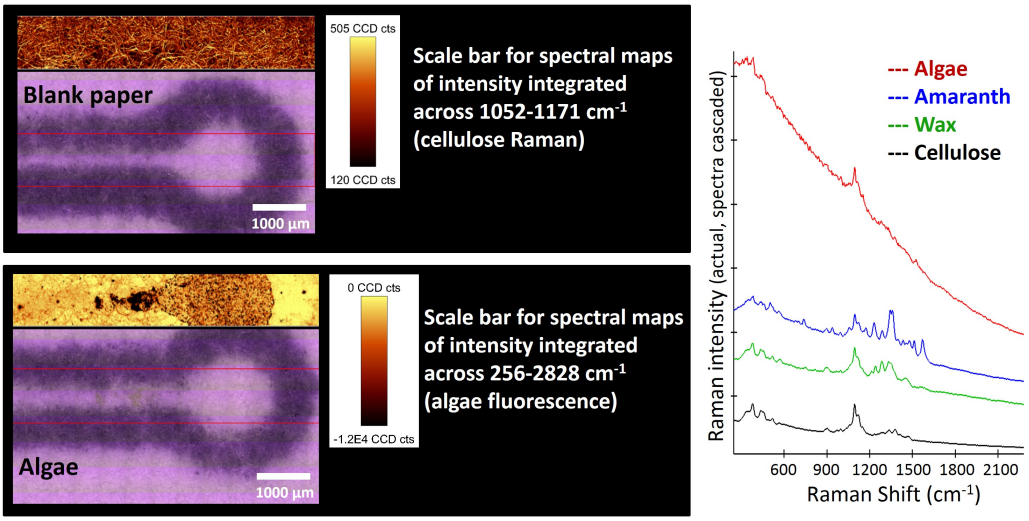

Figure S8. Normal Raman spectral maps image the topography of the cellulose fibers and deposition patterns of fluorescent species such as algal cells, even within the same wax-printed paper channel. Raman spectral images were collected with a 785 nm laser, 10× microscope objective, 300 groves/mm grating, approximately 40 mW of laser power, and 0.05 seconds per spectrum.

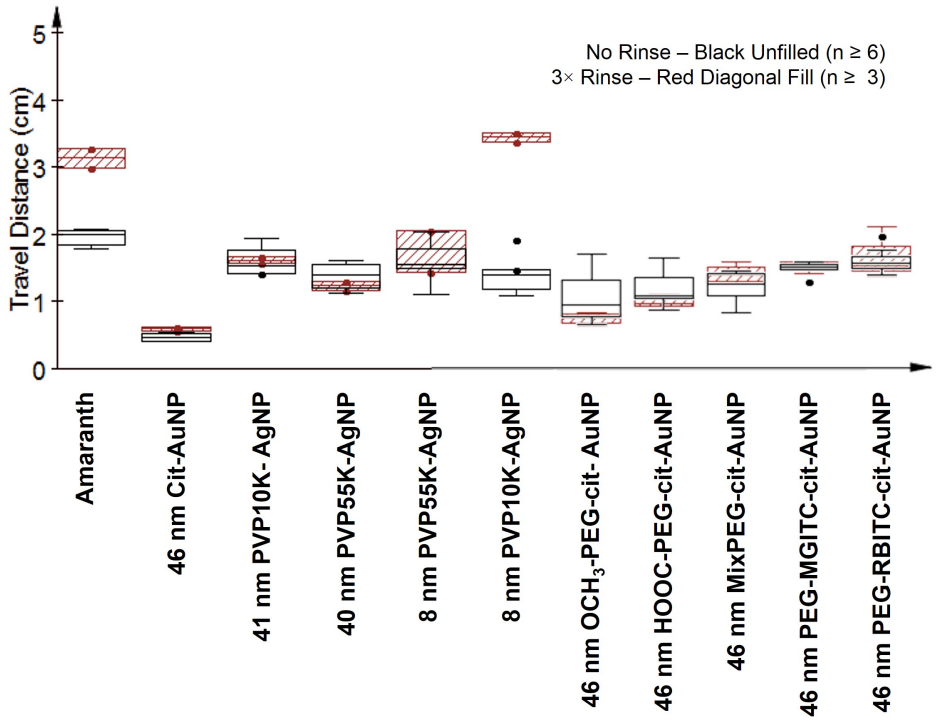

Figure S9. Rinsing three times with 4 µL of nanopure water (12 µL total) had no influence on nanoparticle travel distances except for 8 nm PVP10K-AgNP.

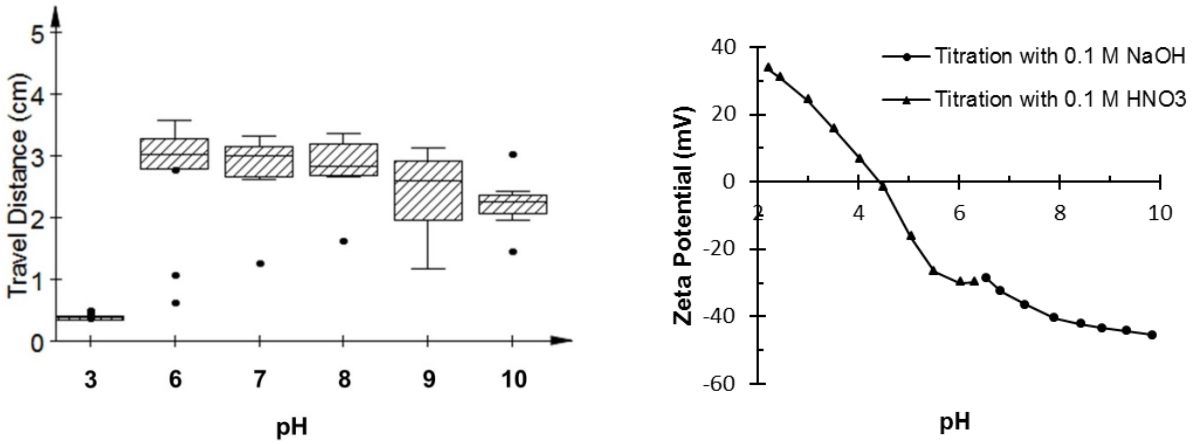

Figure S10. Travel distance (n=9) and zeta potential of 15 nm BSA-cit-AuNP as a function of pH. BSA-cit-AuNP were colloidally unstable at pH 4 and 5; therefore, they were not examined in the channels.

DLVO calculations

DLVO calculations were conducted to examine the attractive and repulsive forces between each nanoparticle and the cellulose surface using zeta potential, hydrodynamic diameter, Hamaker constants estimated from literature values, and ionic strength estimated from conductivity and reagent concentrations employed during synthesis (**Table S6**).[31,32]

Eqn 1 Lifshitz-van der Waals interaction:

$$U_{123}^{LW} = -\frac{A_{123}a_1}{6h}\left(1+\frac{14h}{\lambda}\right)^{-1}$$

Eqn 2 Electrostatic interaction:

$$U_{123}^{EL} = \pi\epsilon_r\epsilon_0 a_1\left[2\zeta_1\zeta_3\ln\left(\frac{1+e^{-\kappa h}}{1-e^{-\kappa h}}\right)+(\zeta_1^2+\zeta_3^2)\ln(1-e^{-2\kappa h})\right]$$

Eqn 3 Inverse Debye length:

$$\kappa = \sqrt{\frac{2N_A e^2\sum c_i z_i^2}{\epsilon_r\epsilon_0 k_B T}}$$

Table S6. DLVO model parameters.[32]

Eqn	Description	Symbol	Value	Units
U_{123}^{LW}	Hamaker constant between particle surface 1 and flat plate surface 3 separated by aqueous medium 2	A_{123}	Estimated (See Table S8)	N m
	Radius of particle (surface) 1	a_1	Measured hydrodynamic diameter (z-average)	m
	Distance between surface 1 and surface 3	h	Variable	m
	Characteristic wavelength of the dielectric	λ	0.0000001	m
U_{123}^{EL}	pi	π	3.141592654	
	Permittivity of the vacuum	ε_0	8.85×10^{-12}	F m
	Relative dielectric constant for water @ T (298 K)	ε_r	78.5	
	Surface (zeta) potential of particle surface 1	ζ_1	Measured	NmC^{-1}
	Surface (zeta) potential of flat plate surface 3 (cellulose literature value)[22,33]	ζ_3	-0.0377	NmC^{-1}
K	Avogadro's Number	N_A	6.022×10^{23}	mol^{-1}
	Elementary charge	e	1.602×10^{-19}	C
	Ionic strength estimated from conductivity[34]	$\Sigma c_i z_i^2$	Measured indirectly (See Table S8)	mol/m^3
	Boltzmann's Constant	k_B	1.381×10^{-23}	J/K
	Temperature	T	298	K
	Inverse Debye length	κ	calculated	m^{-1}

Ionic strength

Nanoparticles are often incorporated into μPADs immediately after synthesis, such that ionic strength is not directly controlled.[35-39] However, ionic strength in nanoparticle solutions varies drastically depending upon the synthesis procedure employed. For instance, the reaction flask in which 15 nm cit-AuNP are produced contains 4 mM Cl^-, 3.9 mM Na^+, and 3.9 mM citrate at various states of oxidation in addition to Au, while PVP-AgNP production involves centrifugation steps to remove excess reagents. Hence, ionic strength values were inferred from reagents used, synthesis protocols, and conductivity measurements converted to ionic strength with a pre-factor of 1.27×10^{-6}.[34] Values were compared to determine reasonable DLVO inputs (**Table S7**).

Table S7. Ionic strength was estimated from conductivity measurements, synthesis protocols, and reagent concentrations.

Sample	Conductivity (mS/cm)	Ionic strength from pre-factor (mM)	Ionic strength from synthesis procedure (mM)	Ionic strength used for DLVO (mM)
15 nm cit-AuNP	0.4	0.5	<13	0.5
46 nm cit-AuNP	0.3	0.4	<2	0.3
15 nm BSA-cit-AuNP			<13	0.5
46 nm BSA-cit-AuNP	0.2	0.2	<2	0.3
64 nm BSA-cit-AuNP	0.2	0.2	<2	0.3
46 nm OCH_3-PEG-cit-AuNP	0.002	0.002	0.0002	0.007
46 nm COOH-PEG-cit-AuNP	0.002	0.003	0.0002	0.007
46 nm OCH_3/COOH-PEG-cit-AuNP	0.002	0.003	0.0002	0.007
46 nm MixPEG-MGITC-cit-AuNP	0.02	0.02	0.0002	0.007
46 nm MixPEG-RBITC-cit-AuNP	0.004	0.005	0.0002	0.007
46 nm DNA-MixPEG-MGITC-cit-AuNP	0.009	0.01	0.0002	0.007
40 nm PVP10K-AgNP			0.0002	0.007
40 nm PVP55K-AgNP			0.0002	0.007
8 nm PVP55K-AgNP			0.0002	0.007
8 nm PVP10K-AgNP			0.0002	0.007

Hamaker constants

Hamaker constants were calculated using a combined relations equation,

$$A_{132} = (A_{11}^{0.5} - A_{33}^{0.5})(A_{22}^{0.5} - A_{33}^{0.5})$$

and literature values (**Table S8**).[32] The combining relations equation breaks down in aqueous systems for which non-dispersive forces dominate, but because alternatives require parameters that are not widely available, the equation is often used as a reasonable estimate.[32,40]

Table S8. Hamaker constant DLVO inputs. A_{11} represents the Hamaker constant of medium 1 interacting with itself across a vacuum. A_{132} was computed with the equation $\boldsymbol{A_{132} = (A_{11}^{0.5} - A_{33}^{0.5})(A_{22}^{0.5} - A_{33}^{0.5})}$ and represents the Hamaker constant of medium 1 interacting with medium 2 across medium 3.[32,40]

Medium	Hamaker constant A_{11} or A_{132} (J)	Used to create Figure 4 for the nanoparticles listed	Reference
Water	3.7×10^{-20}		[32]
Cellulose	8.4×10^{-20}		[41-43]
Au bulk	4.5×10^{-19}		[44-46]
Ag bulk	4.0×10^{-19}		[44,45]
10 nm AgNP	2.1×10^{-19}		[47]
50 nm AgNP	1.6×10^{-19}		[47]
Polymer (general estimate)	6×10^{-20}		[48,49]
BSA	2×10^{-20}		[50-52]
DNA	6.8×10^{-20}		[53,54]
$\mathbf{A_{cellulose\text{-}water\text{-}AuNP}}$	4.69×10^{-20}	Cit-AuNP	calculated
$\mathbf{A_{cellulose\text{-}water\text{-}AgNP40nm}}$	1.97×10^{-20}		calculated
$\mathbf{A_{cellulose\text{-}water\text{-}AgNP8nm}}$	2.58×10^{-20}		calculated
$\mathbf{A_{cellulose\text{-}water\text{-}polymer}}$	5.1×10^{-21}	PVP-AgNP, PEG-cit-AuNP	calculated
$\mathbf{A_{cellulose\text{-}water\text{-}BSA}}$	-5.0×10^{-21}	BSA-cit-AuNP	calculated
$\mathbf{A_{cellulose\text{-}water\text{-}DNA}}$	6.7×10^{-21}	DNA-PEG-cit-AuNP	calculated

Hamaker constant estimates require knowledge of the wavelength dependent dielectric value for each media.[32,41] AuNP and AgNP do not have the same dielectric properties as their bulk counterparts; therefore, Hamaker constant values are expected to be different. The Hamaker constants as a function of nanoparticle size estimated by Pinchuk were used for AgNP, but these values have not been previously computed for AuNP.[47]

We note that when Hamaker constants for metal core materials were applied rather than Hamaker constants of the surface coatings, several particles experimentally contradicted DLVO predictions, placing them in the upper left corner of **Figure 4**, including 15 nm BSA-cit-AuNP at pH >6 and PVP-AgNP. Although it is standard procedure to apply the Hamaker constant of the bulk metal core material rather than the nanoparticle itself or the surface coating when computing van der Waals interaction energies, DLVO calculations were evaluated using both the nanoparticle metal core Hamaker constants as well as that of the surface coating material. In colloidal systems for which DLVO was developed, it was typically safe to assume that the bulk material was that of the particle core;[32] however, for nanomaterials on the order of 15-64 nm with surface coatings nearly doubling the hydrodynamic diameter, the metal core comprises

much less than 50% of the particle volume, and thus cannot necessarily be considered the "bulk". Hamaker constants model van der Waals forces that work across short distances, and although it is generally assumed that the van der Waals forces due to the stabilizing coating are negligible at large distances, at a separation distance equal to the coating thickness the properties of the coating dominate.[32] The particle coatings analyzed herein are not trivial in size, as demonstrated by their molecular weights and the final hydrodynamic diameters (**Table 1**). Therefore, it is safer to assume coating properties are significant, arguably more so than the nanoparticle core.

A negative Hamaker constant for the interaction of a particle with a cellulose surface through water (A_{132}) is computed for 15 nm BSA-cit-AuNP at pH 8 when the Hamaker constant for BSA interacting with itself in a vacuum ($A_{11}=2\times10^{-20}$ J) is applied rather than that of bulk Au (**Table S8**).[50-52] A negative A_{132} is produced when A_{11} for the particle is below that of water (3.7×10^{-20}), as is the typical A_{11} of a protein ($1\text{-}1.5\times10^{-20}$ J).[32,55] The van der Waals attractive force never overcomes the electrostatic repulsion when the BSA Hamaker constant is applied to the DLVO model rather than that of Au bulk for the 15 nm BSA-cit-AuNP at pH 8 (**Figure S11A**), and the DLVO model predicts the experimental data despite the neglect of steric stabilization or Lewis acid-base forces in the model. Using the BSA Hamaker constant does not significantly influence the DLVO model output for pH 3 BSA-cit-AuNP of any size until a separation distance less than 0.1 nm (shorter than a carbon-carbon bond length) because the zeta potential of the nanoparticles is positive (**Figure S11B-C**). The BSA surface coating properties appear to be important in this case because the coating is thick in comparison to the particle size and the range of van der Waals forces and the BSA dictates charge as a function of pH.[32]

BSA NP travel can be logically explained by the surface charge alone. At pH >6 BSA-cit-AuNP have a positive surface charge, such that electrostatic forces between the particles and cellulose are attractive; therefore, travel of the nanoparticles is prevented in the negatively charged cellulose (**Figure S10**).[22,33,56] However, at pH >6, the zeta potential of BSA-cit-AuNP is negative, so the particles travel with the aqueous mobile phase rather than immediately depositing in the cellulose. The DLVO model does not predict the dramatic difference in transport distance for pH 3 vs. pH 6 BSA-cit-AuNP, unless the BSA Hamaker constant is used.

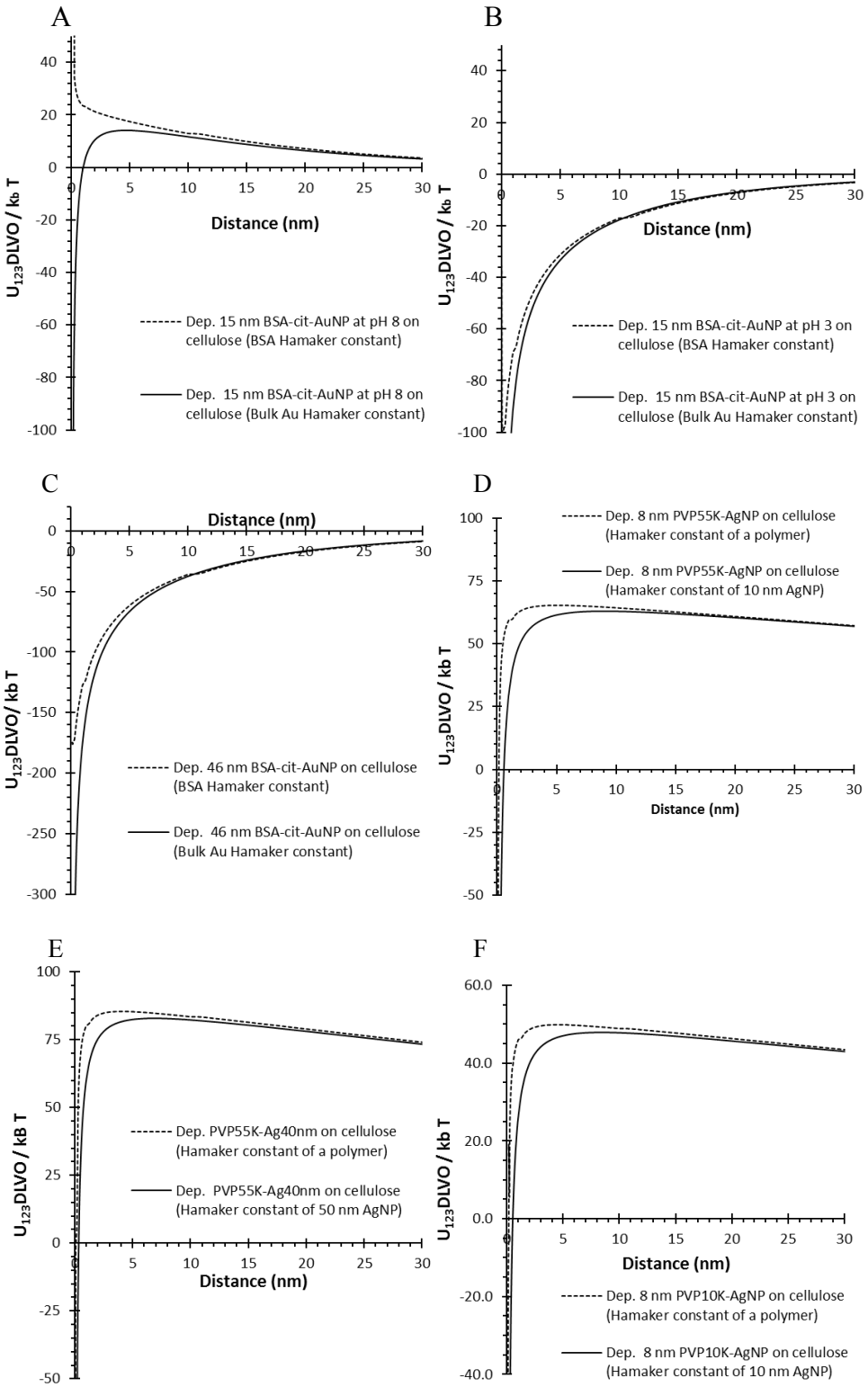

Figure S11. DLVO interaction energies computed using Hamaker constant values for the metal core (solid line) or for the surface coating (dotted line). A) 15 nm BSA-cit-AuNP, pH 8. B) 15 nm BSA-cit-AuNP, pH 3. C) 46 nm BSA-cit-AuNP. D) 8 nm PVP55K-AgNP. E) 40 nm PVP55K-AgNP. F) 8 nm PVP10K-AgNP.

For the interaction of PVP-AgNP with cellulose, replacing the Hamaker constant (A_{11}) of AgNP used to model the PVP-AgNP with a value an order of magnitude smaller (a reasonable value for a polymer)[48,49] reduces A_{132} by an order of magnitude and increases the DLVO interaction energy barrier very slightly. A more significant effect of applying a polymer Hamaker constant is that the van der Waals attractive force does not overcome the electrostatic repulsive force until the particle is closer to the surface (1-3 nm as opposed to 3-5 nm), and the interaction between the PVP-AgNP and cellulose does not become attractive overall until a distance just over 0.1 nm (**Figure S11D-F**). DLVO suggests that electrostatic repulsion forces dominate until the PVP-AgNP approach within a typical bond length. Sterically, it is not likely that the particle would approach within this distance. Therefore, as observed, it is logical that the particles are not deposited in the cellulose.

REFERENCES

1. Hull, M.S.; Chaurand, P.; Rose, J.; Auffan, M.; Bottero, J.Y.; Jones, J.C.; Schultz, I.R.; Vikesland, P.J., Filter-Feeding Bivalves Store and Biodeposit Colloidally Stable Gold Nanoparticles. *Environ. Sci. Technol.* **2011,** *45*, 6592-6599.
2. Ao, L.M.; Gao, F.; Pan, B.F.; Cui, D.X.; Gu, H.C., Interaction between Gold Nanoparticles and Bovine Serum Albumin or Sheep Antirabbit Immunoglobulin G. *Chin. J. Chem.* **2006,** *24*, 253-256.
3. Qian, X.; Peng, X.-H.; Ansari, D.O.; Yin-Goen, Q.; Chen, G.Z.; Shin, D.M.; Yang, L.; Young, A.N.; Wang, M.D.; Nie, S., In Vivo Tumor Targeting and Spectroscopic Detection with Surface-Enhanced Raman Nanoparticle Tags. *Nat. Biotechnol.* **2008,** *26*, 83-90.
4. Kennedy, A.J.; Hull, M.S.; Bednar, A.J.; Goss, J.D.; Gunter, J.C.; Bouldin, J.L.; Vikesland, P.J.; Steevens, J.A., Fractionating Nanosilver: Importance for Determining Toxicity to Aquatic Test Organisms. *Environ. Sci. Technol.* **2010,** *44*, 9571-9577.
5. Ma, R.; Levard, C.; Marinakos, S.M.; Cheng, Y.; Liu, J.; Michel, F.M.; Brown, G.E., Jr.; Lowry, G.V., Size-Controlled Dissolution of Organic-Coated Silver Nanoparticles. *Environ. Sci. Technol.***2012,** *46*, 752-759.
6. Haiss, W.; Thanh, N.T.; Aveyard, J.; Fernig, D.G., Determination of Size and Concentration of Gold Nanoparticles from UV-Vis Spectra. *Anal. Chem.* **2007,** *79*, 4215-21.
7. Gao, P.; Weaver, M.J., Metal-Adsorbate Vibrational Frequencies as a Probe of Surface Bonding: Halides and Pseudohalides at Gold Electrodes. *J. Phys. Chem.* **1986,** *90*, 4057-4063.
8. Jeffrey, M.I.; Watling, K.; Hope, G.A.; Woods, R., Identification of Surface Species That Inhibit and Passivate Thiosulfate Leaching of Gold. *Miner. Eng.* **2008,** *21*, 443-452.
9. Gao, P.; Weaver, M.J., Surface-Enhanced Raman Spectroscopy as a Probe of Adsorbate-Surface Bonding: Benzene and Monosubstituted Benzenes Adsorbed at Gold Electrodes. *J. Phys. Chem.* **1985,** *89*, 5040-5046.
10. Chowdhury, J.; Ghosh, M., Concentration-Dependent Surface-Enhanced Raman Scattering of 2-Benzoylpyridine Adsorbed on Colloidal Silver Particles. *J. Colloid Interface Sci.* **2004,** *277*, 121-127.
11. Ravindranath, S.P.; Henne, K.L.; Thompson, D.K.; Irudayaraj, J., Raman Chemical Imaging of Chromate Reduction Sites in a Single Bacterium Using Intracellularly Grown Gold Nanoislands. *ACS Nano* **2011,** *5*, 4729-4736.
12. Bozzini, B.; Romanello, V.; Mele, C., A SERS Investigation of the Electrodeposition of Au in a Phosphate Solution. *Surf. Coat. Technol.* **2007,** *201*, 6267-6272.
13. Joo, S.W.; Han, S.W.; Kim, K., Adsorption Characteristics of 1,3-Propanedithiol on Gold: Surface-Enhanced Raman Scattering and Ellipsometry Study. *J. Phys. Chem. B* **2000,** *104*, 6218-6224.
14. Jing, C.; Fang, Y., Experimental (SERS) and Theoretical (DFT) Studies on the Adsorption Behaviors of L-Cysteine on Gold/Silver Nanoparticles. *Chem. Phys.* **2007,** *332*, 27-32.
15. Zhang, D.; Neumann, O.; Wang, H.; Yuwono, V.M.; Barhoumi, A.; Perham, M.; Hartgerink, J.D.; Wittung-Stafshede, P.; Halas, N.J., Gold Nanoparticles Can Induce the

Formation of Protein-Based Aggregates at Physiological pH. *Nano Lett.* **2009,** *9*, 666-671.
16. Carrilho, E.; Martinez, A.W.; Whitesides, G.M., Understanding Wax Printing: A Simple Micropatterning Process for Paper-Based Microfluidics. *Anal. Chem.* **2009,** *81*, 7091-7095.
17. Lu, Y.; Shi, W.; Jiang, L.; Qin, J.; Lin, B., Rapid Prototyping of Paper-Based Microfluidics with Wax for Low-Cost, Portable Bioassay. *Electrophoresis* **2009,** *30*, 1497-1500.
18. Martinez, A.W.; Phillips, S.T.; Whitesides, G.M.; Carrilho, E., Diagnostics for the Developing World: Microfluidic Paper-Based Analytical Devices. *Anal. Chem.* **2010,** *82*, 3-10.
19. Breton, M.P.; Malhotra, S.L.; Kovacs, G.J. Ink Compositions. US Patent 6,593,398, July 15, 2003.
20. Malhotra, S.L.; Wong, R.W.; Breton, M.P. Ink Compositions. US Patent 6,461,417, October 8, 2002.
21. Malhotra, S.L.; Wong, R.W.; Breton, M.P. Phase Change Inks. US Patent 6,306,203, October 23, 2001.
22. Pelton, A Model of the External Surface of Wood Pulp Fibers. *Nord. Pulp Pap. Res. J.* **1993,** *08*, 113-119.
23. Tobin, M.C., *Laser Raman Spectroscopy*. John Wiley & Sons, Inc.: Toronto, Canada, 1971; Vol. 35.
24. Movasaghi, Z.; Rehman, S.; Rehman, I.U., Raman Spectroscopy of Biological Tissues. *Appl. Spectrosc. Rev.* **2007,** *42*, 493 - 541.
25. Edwards, H.G.M.; Falk, M.J.P., Fourier-Transform Raman Spectroscopic Study of Unsaturated and Saturated Waxes. *Spectrochim. Acta, Part A* **1997,** *53*, 2685-2694.
26. Mernagh, T.P.; Cooney, R.P.; Johnson, R.A., Raman Spectra of Graphon Carbon Black. *Carbon* **1984,** *22*, 39-42.
27. Kunjappu, J.T., Ink Chemistry. In *Chemistry World*, Royal Society of Chemistry 2003.
28. Zheng, M.; Du, W., Phase Behavior, Conformations, Thermodynamic Properties, and Molecular Motion of Multicomponent Paraffin Waxes: A Raman Spectroscopy Study. *Vib. Spectrosc.* **2006,** *40*, 219-224.
29. Noh, H.; Phillips, S.T., Metering the Capillary-Driven Flow of Fluids in Paper-Based Microfluidic Devices. *Anal. Chem.* **2010,** *82*, 4181-4187.
30. Kreze, T.; Stana-Kleinschek, K.; Ribitsch, V., The Sorption Behaviour of Cellulose Fibres. *Lenzinger Ber.* **2001,** *80*, 28-33.
31. Brant, J.; Labille, J.; Bottero, J.-Y.; Wiesner, M.R., Nanoparticle Transport, Aggregation, and Deposition. In *Environmental Nanotechnology Applications and Impacts of Nanomaterials*, Wiesner, M.R.; Bottero, J.-Y., Eds. McGraw-Hill: New York, 2007; pp 231-294.
32. Israelachvili, J.N., *Intermolecular and Surface Forces*. Third ed.; Elsevier: 2011.
33. Dagaonkar, M.; Majumdar, U., Effect of Fluid Flow, Solution Chemistry and Surface Morphology of Fibrous Material on Colloid Filtration. *J. Eng. Fibers Fabr.* **2012,** *7*, 62-74.
34. Zeng, Y.; Grandner, S.; Oliveira, C.L.P.; Thunemann, A.F.; Paris, O.; Pedersen, J.S.; Klapp, S.H.L.; von Klitzing, R., Effect of Particle Size and Debye Length on Order

Parameters of Colloidal Silica Suspensions under Confinement. *Soft Matter* **2011,** *7*, 10899-10909.
35. Yu, W.W.; White, I.M., A Simple Filter-Based Approach to Surface Enhanced Raman Spectroscopy for Trace Chemical Detection. *Analyst* **2012,** *137*, 168-173.
36. Lee, C.H.; Hankus, M.E.; Tian, L.; Pellegrino, P.M.; Singamaneni, S., Highly Sensitive Surface Enhanced Raman Scattering Substrates Based on Filter Paper Loaded with Plasmonic Nanostructures. *Anal. Chem.* **2011,** *83*, 8953-8958.
37. Abbas, A.; Brimer, A.; Slocik, J.M.; Tian, L.; Naik, R.R.; Singamaneni, S., Multifunctional Analytical Platform on a Paper Strip: Separation, Preconcentration, and Subattomolar Detection. *Anal. Chem* **2013,** *85*, 3977-3983.
38. Ngo, Y.H.; Li, D.; Simon, G.P.; Garnier, G., Gold Nanoparticle–Paper as a Three-Dimensional Surface Enhanced Raman Scattering Substrate. *Langmuir* **2012,** *28*, 8782-8790.
39. Lee, C.H.; Tian, L.; Singamaneni, S., Paper-Based Sers Swab for Rapid Trace Detection on Real-World Surfaces. *ACS Appl. Mater. Interfaces* **2010,** *2*, 3429-3435.
40. Lefévre, G.; Jolivet, A. In *Calculation of Hamaker Constants Applied to the Deposition of Metallic Oxide Particles at High Temperature*, International Conference on Heat Exchanger Fouling and Cleaning VIII, Schladming, Austria, 2009; HMuller-Steinhagen, H.; Malayeri, M.R.; Watkinson, A.P., Eds. Heat Exchanger-Fouling: Schladming, Austria, 2009; pp 120-124.
41. Qing, S., Surface Properties of Cellulose and Cellulose Derivatives: A Review. In *Model Cellulosic Surfaces*, Roman, M., Ed. American Chemical Society: 2009; Vol. 1019, pp 259-289.
42. Holmberg, M.; Berg, J.; Stemme, S.; Ödberg, L.; Rasmusson, J.; Claesson, P., Surface Force Studies of Langmuir–Blodgett Cellulose Films. *J. Colloid Interface Sci.* **1997,** *186*, (2), 369-381.
43. Bergström, L.; Stemme, S.; Dahlfors, T.; Arwin, H.; Ödberg, L., Spectroscopic Ellipsometry Characterisation and Estimation of the Hamaker Constant of Cellulose. *Cellulose* **1999,** *6*, (1), 1-13.
44. Bargeman, D.; van Voorst Vader, F., Van Der Waals Forces between Immersed Particles. *J. Electroanal. Chem. Interfacial Electrochem.* **1972,** *37*, 45-52.
45. Parsegian, V.A.; Weiss, G.H., Spectroscopic Parameters for Computation of Van Der Waals Forces. *J. Colloid Interface Sci.* **1981,** *81*, 285-289.
46. Biggs, S.; Mulvaney, P., Measurement of the Forces between Gold Surfaces in Water by Atomic Force Microscopy. *J. Chem. Phys.* **1994,** *100*, 8501-8505.
47. Pinchuk, A.O., Size-Dependent Hamaker Constant for Silver Nanoparticles. *J. Phys. Chem. C* **2012,** *116*, 20099-20102.
48. Vial, J.; Carré, A., Calculation of Hamaker Constant and Surface Energy of Polymers by a Simple Group Contribution Method. *Int. J. Adhes. Adhes.* **1991,** *11*, 140-143.
49. Bhattacharya, S.N.; Kamal, M.R.; Gupta, R.K., *Polymeric Nanocomposites: Theory and Practice*. Hanser Gardner Publications: 2008.
50. Prasanna, P.R.M.; Chemical, T.U.; Engineering, B., *Application of Secondary Nucleation Models to Polymorphic Systems*. Tufts University: 2008.
51. Srivastava, S.N., Estimate of the Hamaker Constant for Bovine Serum Albumin and a Test of Vold's Theory of the Effect of Adsorption on the van Der Waals Interaction. *Z. Phys. Chem* **1966,** *233*, 237-254.

52. Visser, J., The Concept of Negative Hamaker Coefficients. 1. History and Present Status. *Adv. Colloid Interface Sci.* **1981,** *15*, 157-169.
53. Paillusson, F.; Dahirel, V.; Jardat, M.; Victor, J.M.; Barbi, M., Effective Interaction between Charged Nanoparticles and DNA. *Phys. Chem. Chem. Phys.* **2011,** *13*, 12603-13.
54. Nelson, E.M.; Rochester, U.o., *The Adsorption of DNA onto Unmodified Gold Nanoparticles*. University of Rochester: 2008.
55. Hiemenz, P.C.; Rajagopalan, R., *Principles of Colloid and Surface Chemistry*. Third ed.; CRC Press: Boca Raton, VL, 1997.
56. Stana, K.K.; Pohar, C.; Ribitsch, V., Adsorption of Whitening Agents on Cellulose Fibers — Monitored by Streaming Potential Measurements, Calorimetry and Fluorescence. *Colloid Polym. Sci.* **1995,** *273*, 1174-1178.